Korean J. Chem. Eng., **30**(3), 605-612 (2013)
DOI: 10.1007/s11814-012-0176-z

Mineral behavior of low-temperature lignite ashes under gasification atmosphere

Fenghai Li*, Jiejie Huang, Yitian Fang**,†, and Yang Wang****

*School of Materials Science and Engineering, Henan Polytechnic University, Jiaozuo 454003, China
**Institute of Coal Chemistry, Chinese Academy of Sciences, Taiyuan 030001, China
(*Received 4 February 2012 • accepted 9 October 2012*)

Abstract−To investigate the mineral behavior of lignite ashes under gasification conditions, 450 ºC Xiaolongtan lignite ash samples (XLT-LTA) treated at different temperatures or pressures under reducing atmosphere (H_2/CO_2=1 : 1, volume ratio) have been examined by means of an SC-444 apparatus, a scanning electron microscope with an energy dispersive X-ray detector (SEM-EDX), and by X-ray diffraction (XRD). The results showed the sulfur content in the XLT-LTA to be much higher than that in ashes prepared at 815 ºC, as a result of the release of sulfur dioxide during the oxidization of pyrite. With increasing temperature, the XLT-LTA particles gradually agglomerate and form partially molten surface entities with obvious apertures, and the content of iron and calcium in the congeries or molten parts increases due to the fusion of fine ash particles with the enrichment of iron and the formation of low-temperature eutectics of calcium and iron. An increase of pressure restrains the decomposition of calcite and muscovite, and promotes the formation of iron minerals (e.g., hercynite, cordierite, and sekaninaite) and orthoclase. The content of amorphous material also increases with increasing pressure.

Key words: Mineral Behavior, XLT Lignite, Gasification Condition, Temperature, Pressure

INTRODUCTION

Lignite, which accounts for approximately 40% of global coal reserves, will become increasingly important in energy supplies in the future because of its easy access and low mining costs [1,2]. Inorganic matter present in low-rank coals has adverse effects on its process performance [3,4]. A detailed knowledge of the behaviors of inorganic matter during gasification is of importance to devise strategies for the reduction or elimination of various technological problems (e.g., agglomeration, corrosion, abrasion-erosion, slag formation, and fouling) as well as environmental impacts [5]. During gasification processes, coal ashes pass through a reducing reaction zone. Thus, an understanding of the behaviors of minerals in lignite ashes under a reducing atmosphere is necessary for research and development (R&D) of lignite gasification technology.

The fact that dispersed metals (mineral matter) in low-rank coal act as catalysts for gasification has been explored by many researchers [6-11], and the organically bound calcium in New Zealand lignites has been shown to be responsible for their high reactivity and high hydrogen concentrations during gasification [12]. Matsuoka et al. [13] delineated the transformation mechanisms of alkali and alkaline earth metals in low-rank coal during the gasification process. Sodium silicate results in the formation of slag, and a reduction of temperature or the addition of coarse meta-kaolin at a feed-rate roughly equivalent to its ash content can successfully solve slag formation problems during a high sodium lignite gasification process [14,15].

In recent years, the gasification center of the Institute of Coal Chemistry (ICC), Chinese Academy of Sciences (CAS) has devoted much attention to the R&D of Xiaolongtan lignite (XLT) pressurized fluidized bed ash agglomerate (PFBA) gasification. During the pilot-plant test (the flow sheet of the XLT PFBA pilot plant gasification is shown in Fig. 1), a slag sometimes formed on the inner surface or near the gasifier distribution plate, which affected the gasification efficiency, resulting in defluidization, and even leading to unscheduled shutdown of the whole gasification system [16,17]. The formation mechanism of slag during lignite fluidized-bed gasification, and the methods for its prevention by raw lignite pre-treatment have been explored in previous work [18,19]. Slag formation is strongly related to the behavior of minerals under high temperature and pressure [3,10, 18-20]. XLT ashes contain more calcium and iron minerals, and also the calcium and iron synergistic mechanism is operative in the formation of slag, which increases the likelihood of slag formation. When the Fe_2O_3/CaO (molar ratio) is close to 1, the tendency for ash slagging is maximized [21]. However, little work has been published on mineral behavior of XLT ashes under a reducing atmosphere. Therefore, the purpose of this study has been to explore the mineral behaviors of XLT-LTA ashes under reducing atmosphere (H_2/CO_2=1 : 1, volume ratio) with increasing temperature or pressure. This study may provide some further guidance for R&D of lignite fluidized bed gasification technology.

EXPERIMENTAL

1. Samples Preparation

1-1. Properties of Xiaolongtan Lignite

The XLT samples (air dried basis) used were provided by the gasification center at the ICC, CAS, and originated from Yunnan province, Southwest China. The samples were ground to a particle size of less than 0.200 mm. According to the Chinese standards of coal analyses (GB/T212-2001, GB/T476-2001, GB/T213-2003, GB/T214-1996), proximate and ultimate analyses of the XLT sam-

†To whom correspondence should be addressed.
E-mail: fyt@sxicc.ac.cn

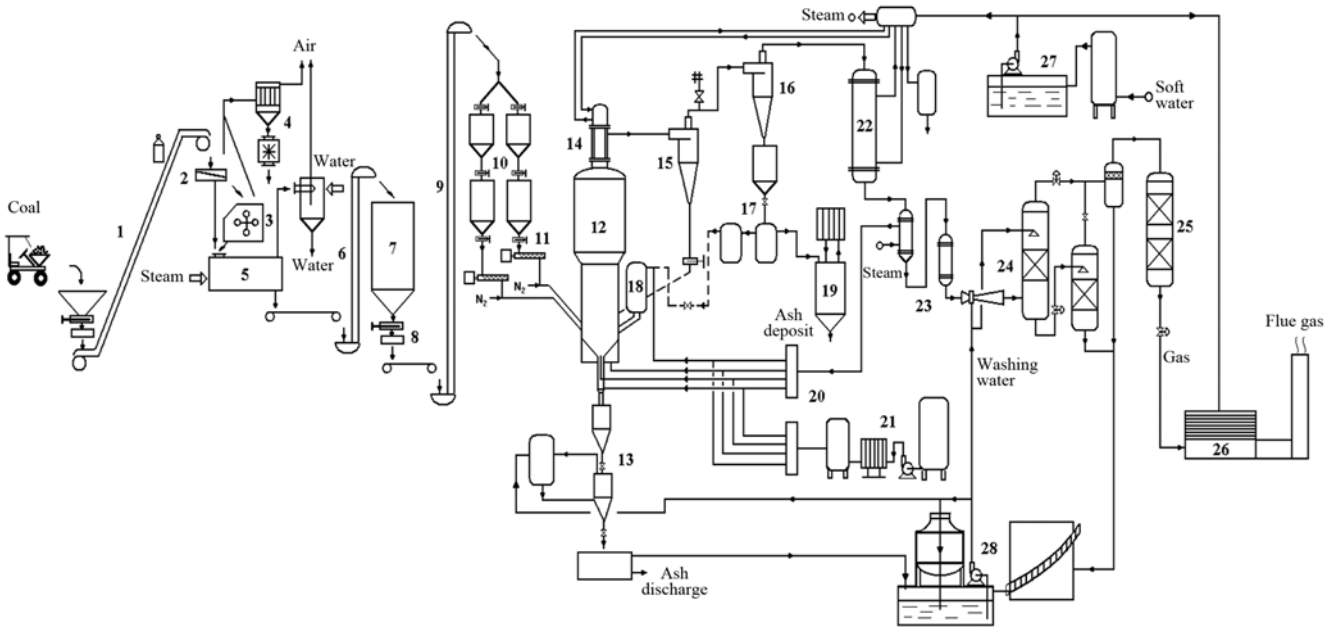

Fig. 1. Flow sheet of the XLT PAFB pilot plant gasification.

1. Belt conveyer
2. Sieving machine
3. Coal crusher
4. Deduster
5. Rotary dryer
6. Conveyer
7. Doal hopper
8. Feeder
9. Bucket elevator
10. Coal lock hopper
11. Rotary feeder
12. Gasifier
13. Ash lock hopper system
14. Heat exchanger
15. 1st Cyclone
16. 2nd Cyclone
17. Fine collection and transport system
18. High temperature fine re-gasifier
19. Fine hopper
20. Steam/oxygen distributors
21. Oxygen supply system
22. Waste heat boiler
23. Steam and soft water pre-heater
24. Water scrubber
25. Desulphurization reactor
26. Gas burner
27. Soft water supply system
28. Washing water cleaning system

ples were performed, and the results are shown in Table 1. Oxygen content was determined by the difference: O_{ad}=100–(C_{ad}+H_{ad}+N_{ad}+$S_{t,ad}$+M_{ad}+A_{ad}), as also listed in Table 1. The ash compositions were determined following analytical methods set out in the Chinese standard GB/1574-2007 for coal, coke, water coal slurry, and gangue. The ash fusion temperature (AFT) under reducing atmosphere (H_2/CO_2=1 : 1, volume ratio) was tested and the results are presented in Table 2. From Table 2, it can be observed that the content of calcium oxide and sulfur trioxide in the XLT ashes is very high, and as expected its AFT is comparatively low.

Table 1. Proximate and ultimate analyses of XLT

Proximate analyses on air dried basis (%)	
Moisture	11.64
Volatile matter	35.56
Ash	8.95
Fixed carbon	43.85
Ultimate analyses on air dried basis (%)	
Carbon	56.65
Hydrogen	3.36
Nitrogen	1.12
Sulfur[a]	1.07
Oxygen[b]	17.21

[a]Total sulfur
[b]By difference

1-2. Preparation of XLT Low Temperature Ash Samples

The preparation procedure for XLT low temperature ashes (XLT-LTA) was as follows: The XLT sample (1.00 g) was first placed in a ceramic crucible, which was in turn placed in a muffle furnace; the muffle furnace was heated from room temperature to 450 °C within 30 min, and the temperature was kept at 450 °C for 24 h. Thereafter, the sample was removed and immediately immersed in iced water; the quenching time was typically no more than 10 s [22]. Phase transformation and segregation of the crystals was prevented by this rapid cooling [23]. The quenched sample was placed in a vacuum oven at 105 °C for 36 h, and crushed to a particle size of

Table 2. Composition of ash sample and its AFT

Constituent	SiO_2	Al_2O_3	Fe_2O_3	CaO	MgO	SO_3	K_2O	Na_2O	TiO_2	P_2O_5
Composition (wt%)	33.14	17.56	8.95	21.64	1.79	13.16	0.99	0.94	1.44	0.28
AFT[a]	DT		ST			HT		FT		
Temperature/°C	1096		1158			1169		1189		

[a]DT - deformation temperature; ST - soften temperature; HT - hemispherical temperature; FT - flow temperature

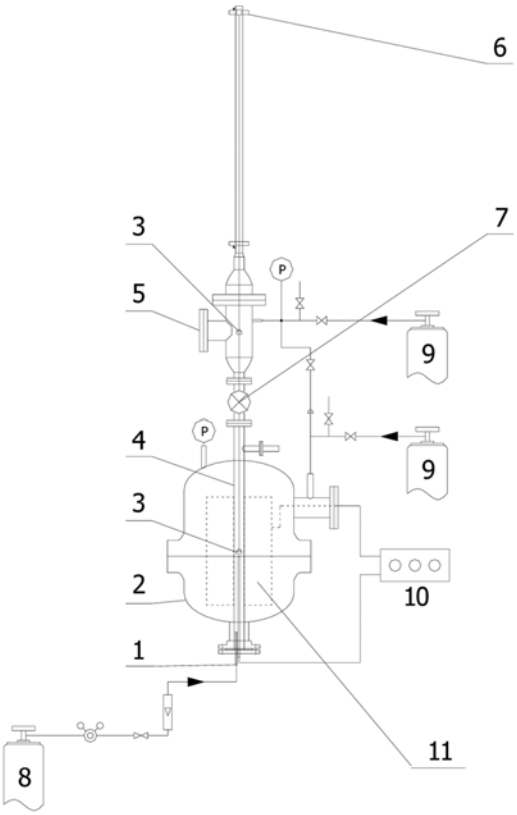

Fig. 2. Schematic diagram of pressurized fixed bed furnace.

1. Gas inlet	7. Ball valve
2. Pressure vessel	8. Reaction gas (H_2/CO_2=1 : 1, volume ratio)
3. Quartz crucible	
4. Reaction pipe	9. N_2
5. Sampling entrance	10. Temperature controller
6. Magnet	11. Furmace

less than 0.074 mm. All samples were stored in a cabinet dryer before measurement.

1-3. Preparation of XLT-LTA under Different Temperatures or Pressures

The ash samples were prepared in a pressurized fixed-bed reactor (Fig. 2), which has been described in detail elsewhere [24]. The depth of the XLT-LTA samples in the crucible was no more than 5 mm, and the external diffusion effect was tested for, and eliminated by, increasing the gas velocity. Based on the temperature at which a slag formed and the operational pressures in the pilot plant at the ICC, CAS, under the conditions of a reducing atmosphere (H_2/CO_2=1 : 1) and a residence time of 15 min, two series of ash samples were prepared: one comprised samples obtained at different temperatures (700, 750, 800, 850, 900, 950, 1000, and 1050 °C) at ambient pressure, while the other comprised samples obtained at different pressures (0.2, 0.4, 0.6, 0.8, and 1.0 MPa) at 900 °C.

The procedure for the preparation of ash samples is briefly outlined as follows. The samples (0.50 g) were placed in a quartz crucible, which was in turn placed in the upper chamber of the reactor. The heaters were activated to increase the temperature to the required value, and then Nitrogen (N_2) was introduced into the pressure vessel and the reactor to displace the air and to increase the pressure to the desired value. Thereafter, a mixture of 50% Hydrogen and 50% carbon dioxide (volume ratio) was introduced into the reactor to displace the N_2. When the conditions were steady, the crucible was lowered into the constant temperature zone by a magnetic force driving system. At the end of the test, the ash samples were elevated to the upper cold chamber, and cooled for about 10 min under N_2 atmosphere. After depressurization of the reactor, the reacted samples were removed and ground to a particle size of less than 0.074 mm for analyses to assess the mineral behavior under a reducing atmosphere.

2. Ash Analytical Methods

A NavaNano 430 scanning electron microscope (SEM) operating at 15.0 kV was employed for observing the morphologies of the samples, and a Sigma energy dispersive X-ray detector (EDX) was used for qualitative elemental identification and semi-quantitative analyses. For SEM observations, the fine ash powders was carefully placed on conducting glue and then coated with gold vapor to make it conductive.

A RIGAKU D/max-rB X-ray powder diffractometer (XRD) employed with Cu Kα radiation (40 kV, 100 mA, Kα_1=0.15408 nm) was used for mineralogical analyses. The samples were scanned with a step size of 0.01° at 5° 2θ/min scanning speed over the range 2θ=15° to 85°.

RESULTS AND DISCUSSION

1. Characterization of XLT-LTA

1-1. Compositions of XLT-LTA

The residual carbon (RC) content in the XLT-LTA was analyzed using an SC-444 apparatus (Leco Corp., St. Joseph, MI), and its remaining constituents were analyzed according to the Chinese standard GB/1574-2007. The results are presented in Table 3. As can be seen from Tables 2 and 3, the sulfur content in the XLT-LTA was much higher than that in ashes prepared at 815 °C, while there were only slight variations in the contents of other components of the ashes. This difference can mainly be attributed to the release of sulfur dioxide due to the oxidization of pyrite during the preparation of the 815 °C ashes.

$$\text{pyrite } (FeS_2)+\text{oxygen } (O_2) \rightarrow \text{magnetite } (Fe_3O_4)+\text{sulfur dioxide } (SO_2)\ [25] \quad (1)$$

$$\text{magnetite } (Fe_3O_4)+\text{oxygen } (O_2) \rightarrow \text{iron oxide } (Fe_2O_3)\ [22] \quad (2)$$

1-2. Surface Morphology of XLT-LTA

An SEM image of XLT-LTA is presented in Fig. 3. It can be seen that the XLT-LTA was mostly composed of many fine irregular granules with a small quantity of large particles, with some fine apertures among the particles.

Table 3. Composition of XLT-LTA (wt%)

Constituent	RC	SiO_2	Al_2O_3	Fe_2O_3	CaO	MgO	SO_3	K_2O	Na_2O	TiO_2	P_2O_5
Composition	3.24	30.17	15.92	8.26	19.69	1.58	17.74	0.98	0.94	1.25	0.23

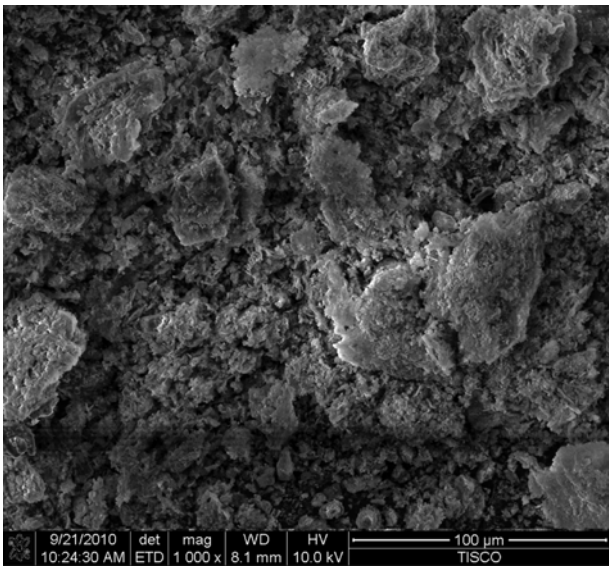

Fig. 3. SEM photo of XLT-LTA.

1-3. Crystal Phases of XLT-LTA

The XLT ash samples were prepared at 450 ºC because at this temperature their mineral constituents are little transformed, and the ashing time is relatively brief. The ratio of the peak heights in the XRD pattern is proportional to the mineral concentrations [26, 27], and for the same mineral, the variation in the diffraction intensity can approximately reflect the variation in its content [28]. The XRD pattern of XLT-LTA is shown in Fig. 4. It can be seen that the XLT-LTA was mainly composed of quartz, anhydrite, and calcite, with small quantities of illite, pyrite, goethite, and kaolinite.

2. Behavior of the Minerals in XLT-LTA with Increasing Temperature

2-1. Surface Morphologies of XLT-LTA at Different Temperatures

To elucidate the precise variations in elemental content in congeries or molten parts of XLT-LTA with increasing temperature, elemental analyses were performed in "spot mode", whereby the beam was localized on a single, manually chosen, circle. SEM images of XLT-LTA and the elemental compositions in congeries or molten parts at different temperatures are shown in Fig. 5. At 800 ºC many irregular fine ash particles were simply stacked together, except for a small quantity of conglutinated particles (Fig. 5(a)), while at 900 ºC, some large particles with fine apertures were formed due to the bonding of some fine ash particles (Fig. 5(b)). At 1,000 ºC, the large particles had been agglomerated, and partially molten surface entities with obvious apertures emerged (Fig. 5(c)). At 1,050 ºC, the surfaces of the entities with some large apertures were melted (Fig. 5(d)). It is also apparent that the XLT ash had been sintered at 900 ºC, almost 200 ºC lower than its deformation temperature (DT) of 1,096 ºC. This is consistent with the results of previous studies, e.g., that the initial melting temperature of ashes can be as low as 200-300 ºC below their DT values [29], and that the agglomeration of six Turkish lignites started at 860-1,060 ºC, again about 125-200 ºC lower than their DT values [30]. Along with the variation in melting temperatures of the ashes, the melting process appears to be accelerated by the presence of calcium through the formation of eutectic mixtures in the FeO-SiO_2-Al_2O_3 and CaO-SiO_2-Al_2O_3 systems [29].

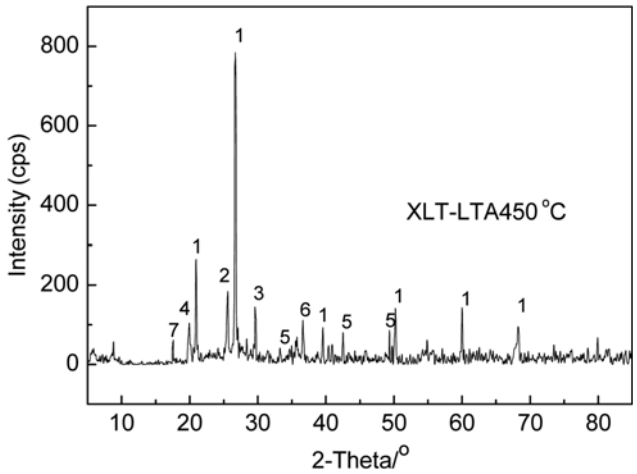

Fig. 4. XRD pattern of XLT-LTA.

1. Quartz (SiO_2)
2. Anhydrate ($CaSO_4$)
3. Calcite ($CaCO_3$)
4. Illite ($KAl_2[(OH)_2AlSi_3O_{10}]$)
5. Pyrite (FeS_2)
6. Goethite (α-FeO(OH))
7. Kaolinite ($Al_4[Si_4O_{10}](OH)_8$)

The main components of ash (SiO_2, Al_2O_3, CaO, and Fe_2O_3) generally comprise more than 85% of its total content. Thus, it is reasonable to predict the properties of ashes from these main components [30]. Based on EDX analyses, the elemental compositions of the congeries or molten parts of XLT-LTA at different temperatures are illustrated in Table 4. It can be seen that the content of iron and calcium increased with increasing temperature. As the XLT-LTA was heated, some fine ash particles first melted and agglomerated due to the enrichment of iron in the fine particles during the formation of ashes [17], leading to the formation of low-melting, adhesive ferro-silicate. Calcium was then assimilated into fayalite structures to form low-temperature eutectic mixtures [31-33], which result in the low DT value of the particles. This offers a possible explanation for the enrichment of iron and calcium in the molten entities with increasing temperature.

2-2. Mineral Transformations of XLT-LTA with Increasing Temperature

Fig. 6 shows the XRD patterns of the main mineral components and their contents in XLT-LTA at different temperatures under reducing atmosphere (H_2/CO_2=1 : 1). It can be seen that XLT-LTA were mostly composed of quartz, illite, anhydrite, goethite, calcite, and magnesium ferrous oxide at 700 ºC. Oldhamite and ferrous magnesium silicate emerged at 800 ºC, and fayalite was indentified at 850 ºC. Anorthite and hercynite were formed at 950 ºC, while the gehlenite appeared at 1,050 ºC.

As the temperature increased, many reactions took place among the various minerals. The diffraction peak of calcite gradually decreased and then disappeared at 850 ºC due to the reaction: calcite ($CaCO_3$) calcium oxide (CaO)+carbon dioxide (CO_2) [29], and the relative content of anhydrate gradually decreased, and oldhamite appeared and then increased due to the following reactions.

anhydrite($CaSO_4$)
→calcium oxide (CaO)+sulfur dioxide (SO_2) [29] (3)

anhydrite ($CaSO_4$)+carbon monoxide (CO)
→oldhamite (CaS)+carbon dioxide (CO_2) (4)

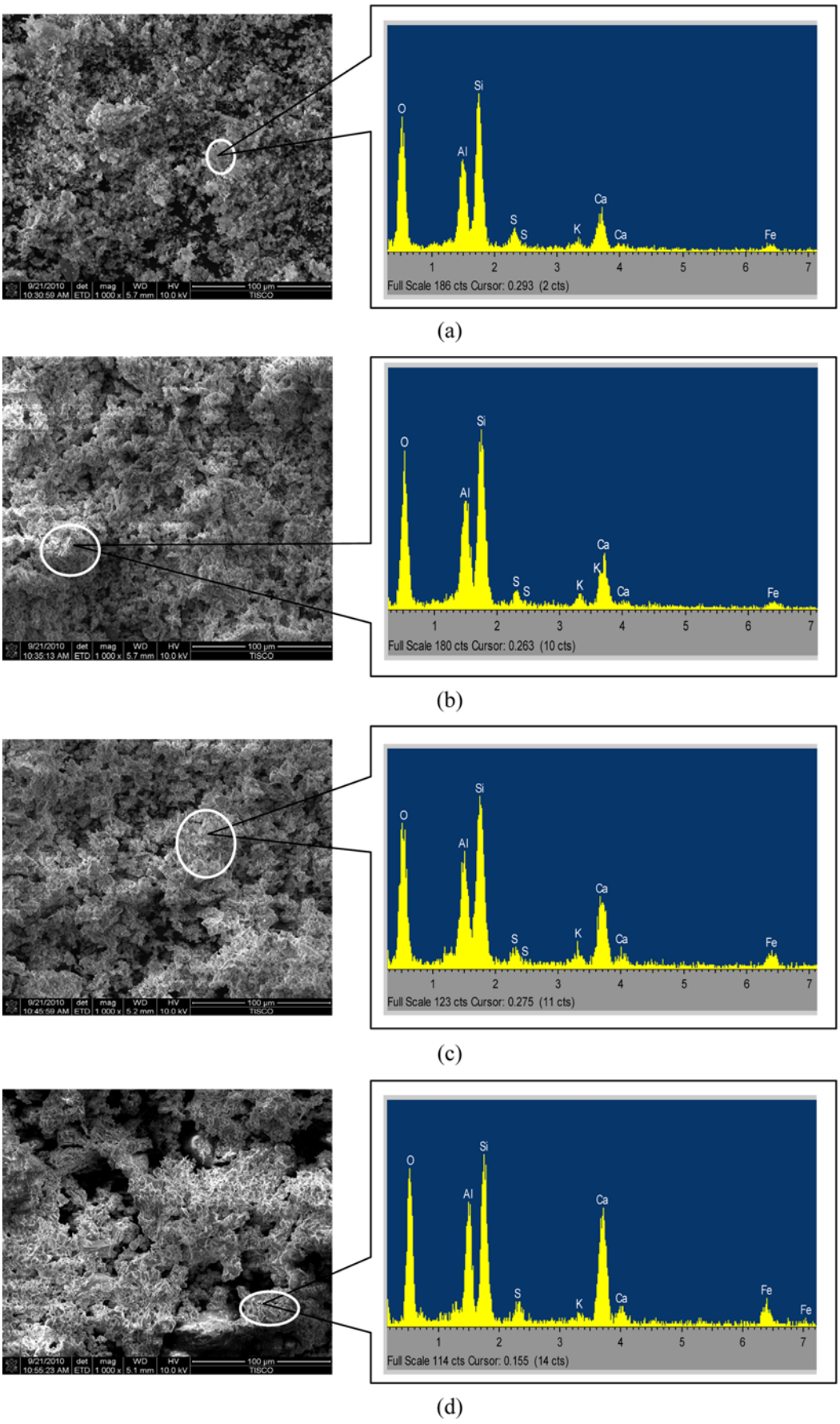

Fig. 5. SEM photos and elemental compositions of XLT-LTA at different temperatures; (a) 800 ºC; (b) 900 ºC; (c) 1,000 ºC; (d) 1,050 ºC.

Table 4. Elemental compositions of XLT-LTA under different temperatures determined by EDX (line weight%)

Element	Temperature/°C			
	800	900	1000	1050
O	55.21	55.39	51.86	44.58
Al	10.87	9.96	8.96	8.89
Si	19.35	18.75	16.29	14.16
S	2.78	1.62	1.73	2.00
K	1.65	2.22	1.63	1.05
Ca	7.83	8.67	12.24	18.54
Fe	2.31	3.38	7.30	10.78

anhydrite ($CaSO_4$)+carbon (C)
→oldhamite (CaS)+carbon dioxide (CO_2) [34] (5)

Under a gasification atmosphere, Fe^{3+} is gradually transformed into Fe^{2+}, which may lead to the formation of magnesium ferrous oxide; the latter can then react with silicon dioxide to generate the ferrous magnesium silicate and oldhamite. Clay minerals may react with partially-oxidized pyrite and calcium oxide to generate silicate glass, which can be melted at 750-760 °C [35]. The reactions of ferrous oxide with mullite, the transformation of kaolinite, lead to the generation of fayalite, which then evolves into hercynite with increasing temperature, and can sometimes lead to the formation of the low-temperature eutectic FeO-FeS [36]. The reaction of calcium oxide with mullite generates anorthite (950 °C), and some anorthite then may evolve into gehlenite (1,050 °C). The interaction of XLT-LTA minerals under reducing atmosphere with increasing temperature may involve the following reactions [23,29,35-37]:

pyrite (FeS_2)→pyrrhotite (FeS)+other sulfides (6)

goethite (α-FeO(OH))→wustite (FeO) (7)

pyrrhotite (FeS)+wustite (FeO)→ferrous sulfide oxide (FeO-FeS) (8)

magnesium ferrous oxide ($(MgO)_{0.77}(FeO)_{0.23}$)+silicon dioxide (SiO_2)
→ferrous magnesium silicate ($Fe_{0.24}Mg_{0.76}SiO_3$) (9)

kaolinite ($Al_2O_3{\cdot}2SiO_2{\cdot}2H_2O$)→mullite ($3Al_2O_3{\cdot}2SiO_2$) (10)

mullite ($3Al_2O_3{\cdot}2SiO_2$)+wusite (FeO)
→fayalite ($2FeO{\cdot}SiO_2$)+hercynite ($FeO{\cdot}Al_2O_3$) (11)

illite ($KAl_2[(OH)_2AlSi_3O_{10}]$)+wustite (FeO)
→almandite ($3FeO{\cdot}Al_2O_3{\cdot}3SiO_2$)
+hercynite ($FeO{\cdot}Al_2O_3$)+leucite ($KAlSi_2O_3$) (12)

calcite ($CaCO_3$)→calcium oxide (CaO) (13)

mullite ($3Al_2O_3{\cdot}2SiO_2$)+calcium oxide (CaO)
→anorthite ($CaO{\cdot}Al_2O_3{\cdot}2SiO_2$) (14)

anorthite ($CaO{\cdot}Al_2O_3{\cdot}2SiO_2$)+calcium oxide (CaO)
→gehlenite ($2CaO{\cdot}Al_2O_3{\cdot}SiO_2$) (15)

3. Behavior of the Minerals in XLT-LTA under Different Pressures

Fig. 7 shows the XRD patterns of the XLT-LTA obtained at 900 °C under at different pressures. The XLT-LTA obtained at 900 °C is mostly composed of quartz, anhydrate, oldhamite, fayalite, and illite

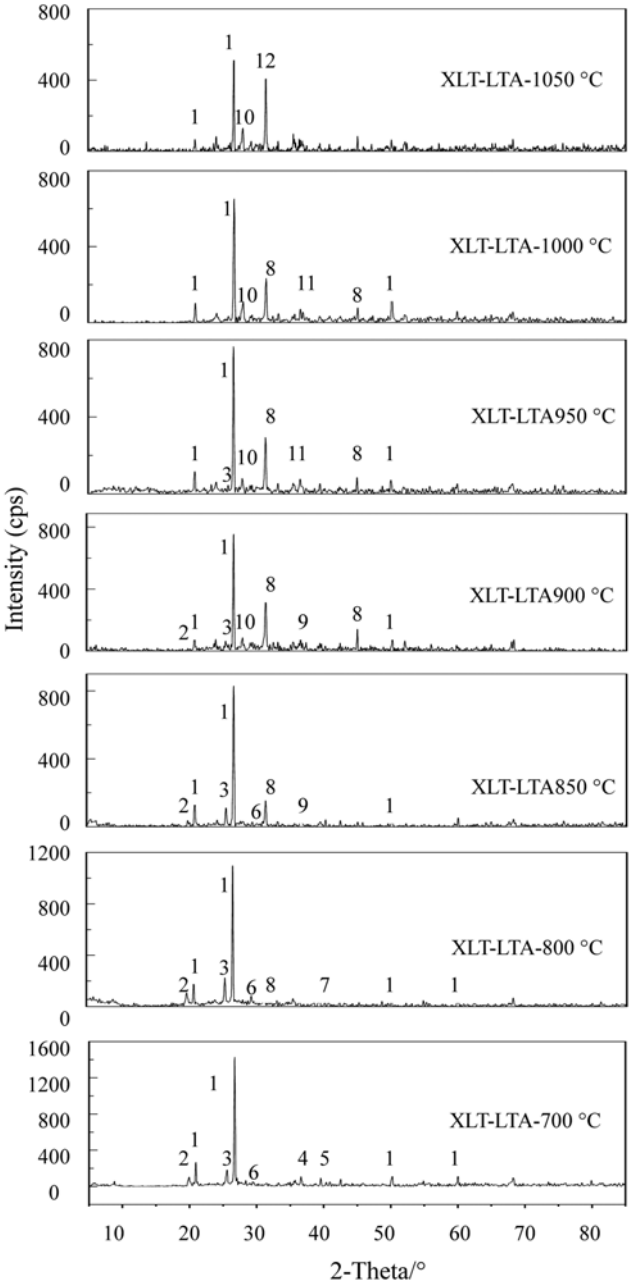

Fig. 6. XRD patterns of XLT-LTA at different temperatures.
1. Quartz (SiO_2)
2. Illite ($KAl_2[(OH)_2AlSi_3O_{10}]$)
3. Anhydrate ($CaSO_4$)
4. Goethite (α-FeO(OH))
5. Magnesium ferrous oxide ($(MgO)_{0.77}(FeO)_{0.23}$)
6. Calcite ($CaCO_3$)
7. Ferrous magnesium silicate ($Fe_{0.24}Mg_{0.76}SiO_3$)
8. Oldhamite (CaS)
9. Fayalite (Fe_2SiO_4)
10. Anorthite ($CaO{\cdot}Al_2O_3{\cdot}2SiO_2$)
11. Hercynite ($FeAl_2O_4$)
12. Gehlenite ($2CaO{\cdot}Al_2O_3{\cdot}SiO_2$)

at ambient pressure (0.02 MPa). Illite is presented in the samples prepared at 900 °C over the whole range of pressures studied, and its content slightly increased with increasing pressure. This is because it begins to react with the wustite at 900 °C (Eq. (12)), and an increase of pressure disfavors this reaction. Calcite and muscovite appear at 0.2 MPa due to increasing pressure preventing their de-

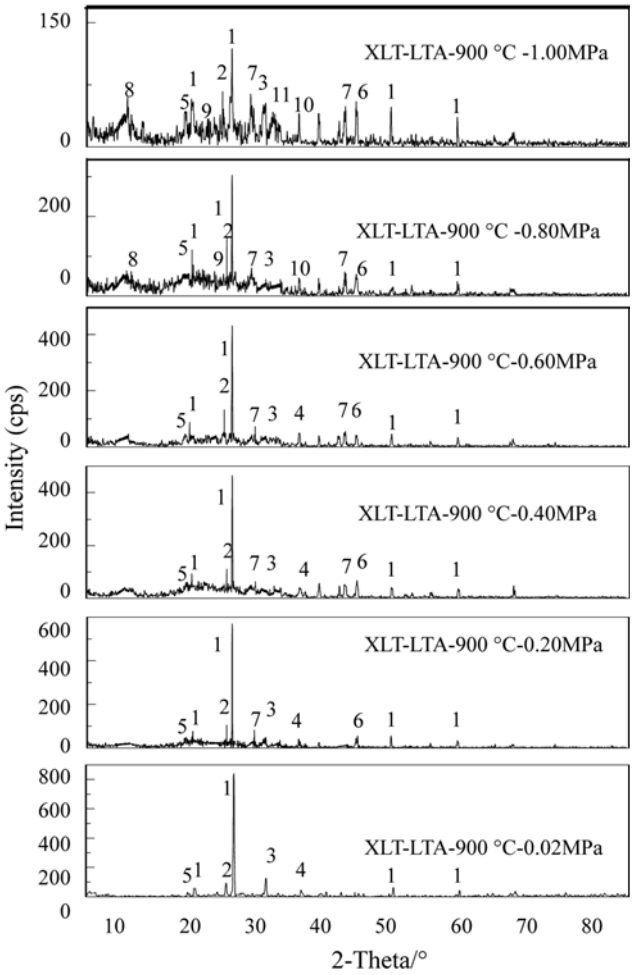

Fig. 7. XRD patterns of XLT-LTA at 900 °C with different pressures.

1. Quartz (SiO_2)
2. Anhydrate ($CaSO_4$)
3. Oldhamite (CaS)
4. Fayalite (Fe_2SiO_4)
5. Illite ($KAl_2[(OH)_2AlSi_3O_{10}]$)
6. Muscovite,syn ($KAl_2Si_3AlO_{10}(OH)_2$)
7. Calcite ($CaCO_3$)
8. Cordierite, ferroan ($(Mg,Fe)_2Al_4Si_5O_{18}$)
9. Orthoclase ($KAlSi_3O_8$)
10. Hercynite ($FeAl_2O_4$)
11. Sekaninaite ($Fe_2Al_4Si_5O_{18}$)

composition. Cordierite and hercynite emerge at 0.8MPa, and sekaninaite appear at 1.0 MPa. With increasing pressure, hercynite, feldspar (e.g., orthoclase and albite), and sekaninaite are formed and their content increases on the basis of their diffraction intensities, as a result of Eqs. (12) and (13), and the following reactions:

$$\text{quartz } (SiO_2)+\text{alumina } (Al_2O_3)+\text{potassium oxide } (K_2O) \rightarrow \text{orthoclas } (KAlSi_3O_8) \quad (16)$$

$$\text{quartz } (SiO_2)+\text{alumina } (Al_2O_3)+\text{sodium oxide } (Na_2O) \rightarrow \text{albite } (NaAlSi_3O_8) \quad (17)$$

$$\text{quartz } (SiO_2)+\text{alumina } (Al_2O_3)+\text{ferrous oxide } (FeO) \rightarrow \text{sekaninaite } (Fe_2Al_4Si_5O_{18}) \quad (18)$$

The abundance of the individual crystalline phases as indicated by XRD analyses was used to estimate the overall chemical composition of the crystalline phase, and the overall composition of the amorphous phase in each case was estimated by subtracting the proportion and inferred composition of the crystalline phases from the bulk ash composition [38]. The content of mineral components of XLT-LTA at 900 °C under different pressures determined by the reference intensity ratio (RIR) is listed in Table 5. The material identified as amorphous materials by XRD techniques was not necessarily of uniform composition within the individual ash samples; it may also have included particle components that were too low in abundance or too small in particle size to be separately identified by X-ray diffraction methods [38].

Table 5. Contents of mineral of XLT-LTA at 900 °C under different pressures determined by RIR

Mineral content (wt%)	Pressure/MPa					
	0.02	0.20	0.40	0.60	0.80	1.00
Quartz	60.09	49.17	43.26	36.17	32.73	28.20
Anhydrate	13.36	13.94	14.45	14.53	14.89	13.23
Oldhamite	10.78	9.28	11.18	11.24	5.38	5.48
Fayalite	8.80	7.23	9.15	9.80	5.15	5.24
Illite	3.12	3.76	4.26	4.54	5.26	3.26
Calcite		9.34	9.84	9.97	5.84	4.83
Muscovite		2.36	2.64	2.78	1.97	2.10
Cordierite, Ferroan					3.27	2.18
Orthoclase					2.38	2.43
Hercynite					2.97	3.04
Sekaninaite						2.43
Glass[a]	3.85	4.92	5.22	10.97	20.16	30.01

[a]Includes both amorphous phase and any carbon (char) components

From Fig. 7 and Table 5, it can also be seen that some low-melting ferrous alumino-silicates (e.g., cordierite and sekaninaite) are formed at 1.0 MPa, which play a binding role in the formation of spherical agglomerates, and assist in the separation of ashes from the gasifier during fluidized-bed gasification. Furthermore, the content of amorphous material clearly increased with increasing pressure on the basis of the distorted baseline in the 2θ range 5-30°.

The effects of pressure on the ash behaviors are mostly due to the shifts in chemical equilibria among the various minerals. Elevated pressure not only restrains the decomposition of calcite and muscovite, but also increases the formation of iron minerals (e.g., hercynite, cordierite, and sekaninaite) and orthoclase, which are likely to form low-temperature eutectic mixtures.

CONCLUSIONS

The mineral behavior of XLT-LTA under a reducing atmosphere at different temperatures and pressures has been studied. From the compositions of XLT-LTA and ash prepared at 815 °C ash, it can be concluded that the sulfur content in the former was much higher than that in the latter as a result of the release of sulfur dioxide during the oxidization of pyrite. With increasing temperature, the XLT-LTA particles gradually agglomerated and formed partially molten surface entities with obvious apertures, and the fusion of fine ash particles with the enrichment of iron and the formation of low-temperature eutectics of calcium and iron led to increases in the contents of iron and calcium in the congeries or molten parts. Due to

the effects of pressure on the positions of various chemical equilibria, increased pressure not only restrained the decomposition of calcite and muscovite, but also promoted the formation of iron minerals (e.g., hercynite, cordierite, and sekaninaite) and orthoclase. Furthermore, the content of amorphous material increased with increasing pressure.

ACKNOWLEDGEMENTS

This work was financially supported by Knowledge Innovation Programs of the Chinese Academy of Science (KGCX2-YW-397), Opening Foundation of State Key Laboratory of coal conversion (J12-13-102), and the National High-Tech R&D Program of China (863 Program, 2008AA050302).

REFERENCES

1. B. L. Chadwick, *Ind. Eng. Chem. Res.*, **38**, 1159 (1999).
2. K. Zhang, C. You and Y. Li, *Korean J. Chem. Eng.*, **29**(4), 540 (2012).
3. S. A. Benson and J. N. Harb, *Energy Fuels*, **7**, 743 (1993).
4. S. A. Benson and P. L. Holm, *Ind. Eng. Chem. Prod. Res. Dev.*, **24**, 149 (1985).
5. C. G. Vassileva and S. V Vassilev, *Fuel Process. Technol.*, **86**, 1297 (2005).
6. H. Liu, C. Luo, M. Toyota, S. Kato, S. Uemiya, T. Kojima and H. Tominaga, *Fuel*, **82**, 523 (2003).
7. M. Grigore, R. Sakurovs, D. French and V. Sahajwalla, *Int. J. Coal Geol.*, **75**, 213 (2008).
8. J. Bai, W. Li, C. Z. Li, Z. Q. Bai and B. Q. Li, J. *Fuel Chem. Technol.*, **37**, 134 (2009).
9. F. I. Muhammad, R. U. Muhammad and K. Kusakabe, *Energy*, **36**, 12 (2011).
10. G. Skodras and G. P. Sakellaropoulo, *Fuel Process. Technol.*, **77-78**, 151 (2002).
11. S. Sun, J. Zhang, X. Hu, P. Qiu, J. Qian and Y. Qin, *Korean J. Chem. Eng.*, **28**, 554 (2009).
12. T. Clemens, D. Gong and S. Pearce, *Int. J. Coal Geol.*, **65**, 235 (2006).
13. K. Matsuoka, T. Yamashita, K. Kuramoto, K. Suzuki, A. Takaya and A.Tomita, *Fuel*, **87**, 885 (2008).
14. R. S. Dahlin, W. W. Peng, M. Nelson, P. Vimalchand and G. H. Liu, *Energy Fuels*, **20**, 2465 (2006).
15. R. S. Dahlin, R. J. Dorminery, W. W. Peng, R. F. Leonard and P. Vimalchand, *Energy Fuels*, **23**, 785 (2009).
16. B. J. Skrifvars, M. Hupa and M. Hiltunen, *Ind. Eng. Chem. Res.*, **31**, 1026 (1992).
17. H. J. Park, N. H. Jung and J. M. Lee, *Korean J. Chem. Eng.*, **28**, 1791 (2011).
18. F. H. Li, J. J. Huang, Y. T. Fang and Y. Wang, *Energy Fuels*, **25**, 273 (2010).
19. F. H. Li, J. J. Huang, Y. T. Fang and Y. Wang, *Fuel*, **90**, 2377 (2011).
20. W. J. Song, L. H. Tang, X. D. Zhu, Y. Q. Wu, Y. Q. Rong, Z. B. Zhu and S. Koyama, *Fuel*, **88**, 297 (2009).
21. S. Su, J. H. Pohi, D. Holcombe and J. A. Hart. *Fuel*, **80**, 1351 (2001).
22. H. X. Li, Y. Ninomiya, Z. B. Dong and M. X. Zhang. *Chinese J. Chem. Eng.*, **14**, 784 (2006).
23. J. Bai, W. Li and B. Q. Li, *Fuel*, **87**, 583 (2008).
24. C. Y. Li, J. T. Zhao, Y. T. Fang and Y. Wang, *Energy Fuels*, **23**, 5099 (2009).
25. J. Tomeczek and H. Palugniok, *Fuel*, **81**, 1251 (2002).
26. S. V. Vassilev, K. Kitano, S. Takeda and T. Tsurue, *Fuel Process. Technol.*, **45**, 27 (1995).
27. J. Yang, B. Xiao and A. R. Boccaccini, *Fuel*, **88**, 1275 (2009).
28. J. C. Van Dyk, S. A. Benson, M. L. Laumb and B. Waaders, *Fuel*, **88**, 1057 (2009).
29. X. J. Wu, Z. X. Zhang, G. L. Piao, X. He, Y. S. Chen, N. Kobayashi, S. Mori and Y. Itaya, *Energy Fuels*, **23**, 2420 (2009).
30. H. Atakül, B. Hilmiðlu and E. Ekinci, *Fuel Process. Technol.*, **86**, 1369 (2005).
31. P. Samaras, E. Diamadopoulos and G. P. Sakellaropoulos, *Fuel*, **75**, 1108 (1996).
32. S. Srinivasachar, J. J. Helble, A. A. Boni, N. Shah, G. P. Huffman and F. E. Huggins, *Prog. Energy Combust. Sci.*, **16**, 293 (1990).
33. J. H. Zhou, X. H. Zhao, W. J. Yang, X. Y. Cao, J. Z. Liu and K. F. Cen, *Proc. CSEE.*, **27**, 31 (2007).
34. E. Wiberg, N. Wiberg and A. F. Holleman, *Inorganic chemistry*, Berlin Academic Press Publications, Germany (2001).
35. R. H. Matjie, Z. Li, C. R. Ward and F. David, *Fuel*, **87**, 857 (2008).
36. V. Marinov, S. P. L. Marinov, L. Lazarov and M. Stefanova, *Fuel Process. Technol.*, **31**, 181 (1992).
37. A. Kondratiev and E. Jak, *Fuel*, **80**, 1989 (2001).
38. C. R. Ward and D. French, *Fuel*, **85**, 2268 (2006).